

Title: Modulation of SARS-CoV-2 spike binding to ACE2 through conformational selection

Authors: Prithwidip Saha,^{1,†} Ignacio Fernandez,^{2,†} Fidan Sumbul,^{1,†} Claire Valotteau,^{1,†} Dorota Kostrz,^{3,†} Annalisa Meola,² Eduard Baquero,² Arvind Sharma,² James R. Portman,³ Francois Stransky,³ Thomas Boudier,^{4,‡} Pablo Guardado Calvo,² Charlie Gosse,^{3,*} Terence Strick,^{3,*} Felix A. Rey,^{2,*} Felix Rico^{1,*}

Affiliations:

¹Aix-Marseille Univ, INSERM, DyNaMo, Turing centre for living systems; Marseille, 13009, France.

² Institut Pasteur, Université Paris-Cité, Structural Virology Unit, CNRS UMR3569; Paris, 75015, France.

³ Institut de Biologie de l'Ecole Normale Supérieure, ENS, CNRS, INSERM, PSL Research University; Paris, 75005, France.

⁴ Aix-Marseille Univ, Turing centre for living systems, Multiengineering platform; Marseille, 13009, France.

* Corresponding authors. Emails: felix.rico@inserm.fr, felix.rey@pasteur.fr, strick@biologie.ens.fr, gosse@ens.fr

† Equal contribution

‡ Present address: Centrale Méditerranée; Marseille, 13013, France.

Abstract:

The first step of SARS-CoV-2 infection involves the interaction between the trimeric viral spike protein (*S*) and the host angiotensin-converting enzyme 2 (*ACE2*). The receptor binding domain (*RBD*) of *S* adopts two conformations: open and closed, respectively, accessible and inaccessible to *ACE2*. Therefore, *RBD* motions are suspected to affect *ACE2* binding; yet a quantitative description of the underlying mechanism has been elusive. Here, using single-molecule approaches, we visualize *RBD* opening and closing and probe the *S/ACE2* interaction. Our results show that *RBD* dynamics affect *ACE2* binding but not unbinding. The resulting modulation is quantitatively predicted by a conformational selection model in which each protomer behaves independently. Our work reveals a general molecular mechanism affecting binding affinity without altering binding strength, helping to understand coronavirus infection and immune evasion.

Main text:

The first step in the entry of SARS-CoV-2 into a target cell is recognition by the viral spike protein (*S*) of the human angiotensin-converting enzyme 2 (*ACE2*) at the plasma membrane of target cells. The *S* protein forms a trimer that undergoes maturation to yield two subunits, *S1* (forming the head of the spike and responsible for recognition) and *S2* (forming the stalk and responsible for subsequent membrane fusion) (1, 2). The receptor binding domain (*RBD*) is part of *S1* and has been shown to adopt two distinct conformations, open and closed (3–9). Only the open *RBD* interacts and forms a complex with *ACE2*. This interaction has been probed using both ensemble and single-molecule binding assays, showing that the isolated *RBD* displays higher affinity for *ACE2* compared with the *RBD* embedded within the *S* trimer (3, 10–17). *RBD* switching between open and closed conformations explain this observation (18). Supporting this idea, it has been shown that the occurrence of *S* variants with mutations away from the receptor binding motif modulates binding to *ACE2* and binding is suppressed when disulfide bonds are introduced to lock *RBD* in the closed conformation (19–24). Microsecond-scale molecular dynamics simulations revealed large conformational changes in *S1* and elucidated the impact of glycans and *RBD*-distal mutations in the closed/open transition pathways (25–28). Experimentally, single-molecule FRET (smFRET) monitored real-time dynamics of labeled *RBD* in *S* trimers, revealing subsecond transition times between up to four conformations attributed to states in which one or multiple *RBDs* are open (29–32). Finally, high-speed atomic force microscopy (HS-AFM) imaging monitored the dynamics of these transitions (17, 33, 34). Although no rate constants were reported, it clearly showcased the potential of this technique. Despite these important advances, various outstanding questions remain, including whether each *RBD* in the trimeric spike opens and closes independently or in coordination with the others, and how the thermodynamics and kinetics of the conformational change affect the affinity of *S* trimers for *ACE2*.

Here, we used HS-AFM imaging to visualize in real-time the conformational dynamics of all three *RBDs* of an *S* trimer, thereby measuring their opening and closing rate constants. We also proved that the *RBD* of each *S* protomer opens and closes independently. We then probed the bond strength of *ACE2* to both the isolated *RBD* and the full-length *S* trimer over a wide range of conditions using complementary approaches: bilayer interferometry (BLI), magnetic tweezers (MT) coupled to junctured-DNA, and HS-AFM-based single-molecule force spectroscopy (HS-FS). All our results consistently showed that the parameters of the energy landscape towards dissociation and the corresponding rate constant at zero force are similar for an isolated *RBD* and for a *RBD* within the *S* trimer. Conversely, we found that the binding of *ACE2* to *S* trimers is modulated by the fast *RBD* conformational changes, which affect both the association rate constant and the affinity. Our data derived from multiple experimental techniques are quantitatively and coherently described by a conformational selection model.

Real-time conformational dynamics of *RBDs*

To quantify *RBD* opening and closing, we imaged *S* trimers on mica surfaces with HS-AFM, at subsecond timescale, nanometer resolution, and in near-physiological conditions (see Materials and Methods) (35). To improve the stability of recombinant *S* trimers, we used two engineered versions of the Wuhan variant, one with mutations at the furin protease cleavage site located between *S1* and *S2* (S_{Wuhan}^{f-}), and the second with a double proline substitution in the loop between the first heptad repeat and the central helix of *S2* (S_{Wuhan}^{2P}), as encoded in various mRNA-based vaccines (2, 3, 5, 36). HS-AFM videos revealed up to three protrusions of 3–5-nm size, stochastically projecting out from the bulbous head of *S* trimers (Fig. 1A, figs. S2–S3 and

supplementary videos). We interpreted them as the signature of *RBD* opening on each *S* protomer, in line with the simulated topographical images derived from cryo-EM structures (37) (Fig. 1A and see Materials and Methods). Thus, four S_i states were identified for the *S* trimer, with $i = 0$ to 3 indicating the number of open *RBDs*. We developed a semi-automatic image analysis routine to process thousands of images (see Materials and Methods and fig. S1), assigning each image to one of four identified states and yielding opening/closing trajectories over time (Fig. 1B).

From these trajectories, we then computed the relative occupancy of each state S_i and displayed them as state density histograms (Fig. 1C). The results for S_{Wuhan}^{f-} and S_{Wuhan}^{2P} revealed that the S_1 state was the most populated, with more than half of the total (52 and 54 %, respectively), followed by the S_0 (34 and 39 %) and S_2 states (10 and 6 %), the S_3 state being the least populated one (<5 %). Particle classification of Wuhan variant *S* trimer structures from cryo-EM agrees with our results (supplementary text S1) (2, 5, 7). We obtained rough estimates of the *RBD* closing equilibrium constants, K_C , by first computing the ratios between the populations of closed and open *RBDs* (Table 1), yielding 2.6 ± 0.6 for S_{Wuhan}^{f-} and 3.3 ± 0.8 for S_{Wuhan}^{2P} . Next, to test the assumption of independent opening between the different protomers, we fitted the state density histograms with a binomial distribution and obtained the probabilities for an *RBD* to be open (p_{open}) (Fig. 1C, Table 1). These measurements confirmed our hypothesis of independence of the transitions. Alternatively, computing K_C as $p_{closed}/p_{open} = 1/p_{open} - 1$ led to 2.5 ± 0.4 and 2.9 ± 0.6 for S_{Wuhan}^{f-} and S_{Wuhan}^{2P} , respectively, in agreement with our rough estimates.

HS-AFM videos also provided access to *RBD* opening/closing dynamics. From the pooled opening/closing trajectories (Fig. 1B), we calculated the probability of transitions from state S_i to state S_j to build transition density plots (TDP, Fig. 1D) (38). The data displayed the diagonal symmetry expected from the detailed balance between conformational transitions at equilibrium. The higher frequencies of transitions for $|j - i| = 1$ (>85 %) are easy to understand given the relative occupancy of the various states. We attributed the uncommon $|j - i| > 1$ transitions to the limited time resolution of HS-AFM.

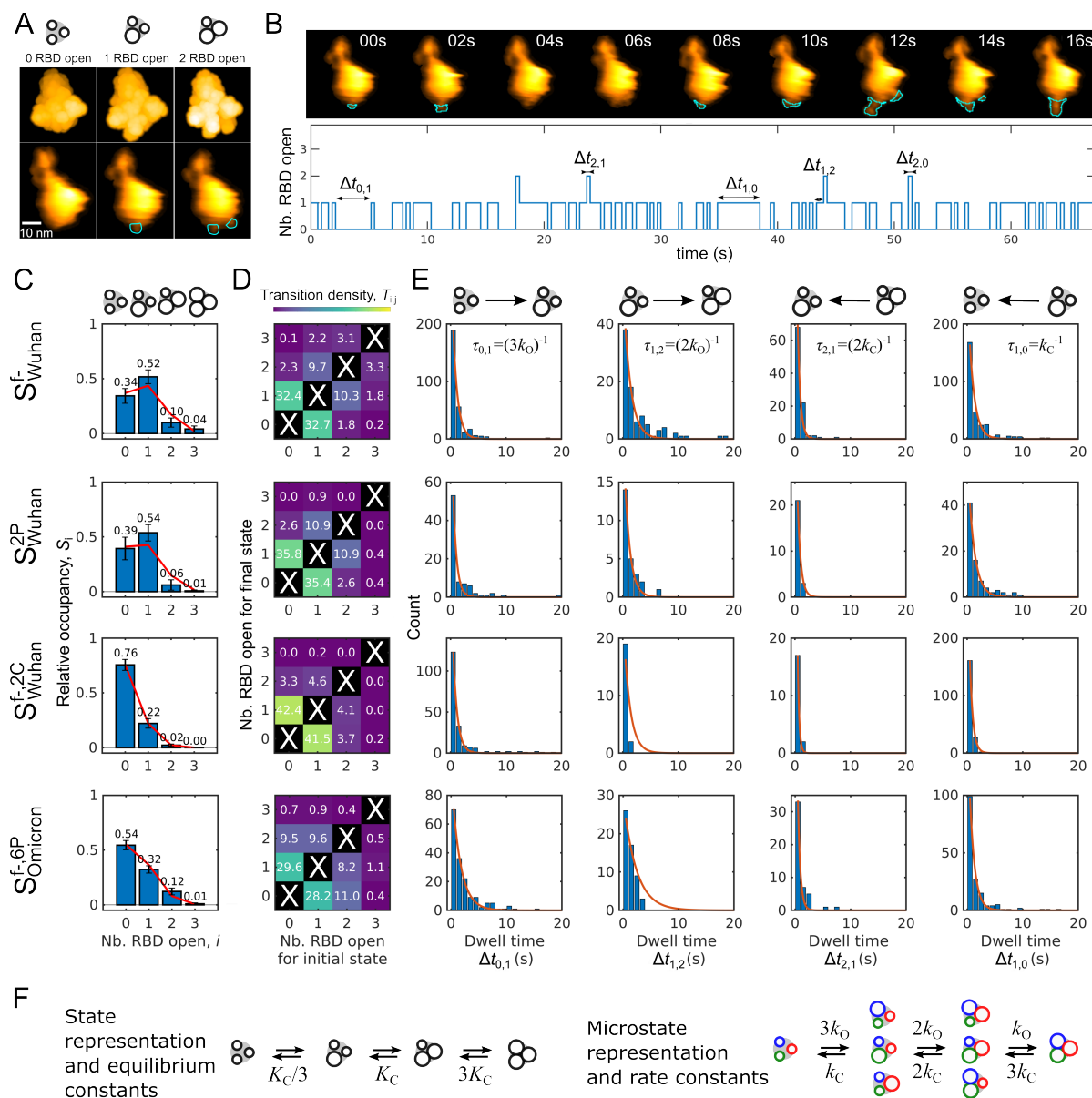


Fig. 1. Single-molecule real-time visualization of the conformational dynamics of RBD opening and closing in S trimers. (A) Top. Simulated HS-AFM topography of an S_{Wuhan}^f trimer immobilized on a mica surface showing 0 to 2 RBDs open (left to right, PDB: 7DDD, 7BNN, and 7BNO, respectively). Bottom. Corresponding experimental images. (B) Top. Representative frames extracted every 2 s from an HS-AFM video showing the opening and closing RBDs (cyan lines). Bottom. Representative trajectory showing the number of RBDs in the open state for one HS-AFM video acquired at 1 fps. (C) Relative occupancy histograms (mean \pm SEM, blue bars) and associated fits to the binomial distribution (red lines) for the four S_i states, i indicating the number of opened RBDs. (D) Transition density plots (TDP) showing the fraction of transition events between the different states. (E) Distributions of the $\Delta t_{i,j}$ dwell times for the four most populated S_i to S_j transitions. Red lines show global fits of exponential decays (see Table 1 for results and table S2 for statistics). (F) Schematic representation of all possible states and microstates for S trimers as well as of all possible transitions. K_C is the RBD closing equilibrium constant, and k_O and k_C are the corresponding opening and closing rate constants, respectively. The RBD coloration for the microstates is pedagogical, the protomers being indistinguishable.

To get quantitative insight into opening and closing kinetics, we generated histograms of the $\Delta t_{i,j}$ dwell times before the four most populated S_i to S_j transitions (representing 85 – 95 % of the total, Fig. 1E). Exponential fitting of the individual histograms yielded $\tau_{i,j}$ characteristic times

of ~ 2 s before opening, and ~ 3 s before closing. Assuming independence between protomers, the observed transition rate constants, $k_{ij} = 1/\tau_{ij}$, are related to the opening and closing rates of single *RBD*, k_O and k_C , by $k_{i,i+1} = (3 - i) \times k_O$ and $k_{i+1,i} = (i + 1) \times k_C$ (Fig. 1F). Thus, we globally fitted the 4 histograms with monoexponential decays with the opening and closing rate constants and four transition amplitudes as free parameters. This yielded opening rates about twice slower than closing rates ($k_O = 0.4 - 0.5$ s $^{-1}$ and $k_C = 0.9 - 1$ s $^{-1}$) for S_{Wuhan}^{f-} and S_{Wuhan}^{2P} (Table 1), *i.e.* the time of an *S* protomer with its *RBD* open is about half of that with the *RBD* closed. Recast in terms of closing equilibrium constants $K_C = k_C/k_O$, we obtained 2.5 ± 1.4 for S_{Wuhan}^{f-} and 1.7 ± 1.4 for S_{Wuhan}^{2P} (Table 1), in agreement with population estimates. Overall, from both thermodynamic and kinetic points of view, the two constructs for the Wuhan spikes we studied do not differ from each other. The similarity of the results of the *f*- and *2P* forms, despite displaying mutations at very different locations along the sequence, suggests that they do not affect the opening and closing of the *RBD*. Our approach allows quantification of effective opening and closing rates for each individual *RBD* in the *S* trimer and suggests conformational changes independent of each other. Population and kinetic analysis lead to similar results and provide a framework that can be applied to other techniques, either from snapshots obtained by cryo-EM single particle analysis (table S1), or transition rates derived from smFRET.

To validate our HS-AFM approach, we imaged the conformational states of construct $S_{Wuhan}^{f-,2C}$, which has D985 and S383 replaced by cysteines, engineered to form a disulfide bond to retain the *RBDs* in the closed state, thereby impairing *ACE2* binding (20, 39, 40). Compared to S_{Wuhan}^{f-} , *RBD* closed states are favored: 76 ± 7 % of all spikes showed no open *RBDs*, 22 ± 4 % displayed one open *RBD*, and 2 ± 1 % displayed two open *RBDs* (Fig. 1C). A similar mutant also presenting the *2P* mutation ($S_{Wuhan}^{f-,2C,2P}$) provided similar results, further confirming our approach and the minor effect of the *2P* mutation (fig. S4, table S2). Although considerably reduced, some degree of *RBD* dynamics is still allowed after the *2C* substitution, suggesting that there is not 100 % disulfide bond formation in this construct, which is consistent with cryo-EM studies (24, 40). Furthermore, while the opening rate remained unchanged, the closing rate was almost twice faster for $S_{Wuhan}^{f-,2C}$ than that of S_{Wuhan}^{f-} (Table 1). The faster rate closing constants of $S_{Wuhan}^{f-,2C}$ are similar to those found in smFRET experiments, suggesting possible intermediate states, not considered in our analysis (supplementary text S1) (29, 32). The probability of an *RBD* to be in the open state in the $S_{Wuhan}^{f-,2C}$ construct was 0.1 and K_C was estimated to be between 5 and 11 (Table 1). While the K_C values obtained from population and kinetic analyses were similar, their accuracy was limited by the frame rate of our HS-AFM imaging (1-2.5 frame per second), which was similar to the closing rate constant. Therefore, for $S_{Wuhan}^{f-,2C}$, the population analysis might be more accurate.

One of the most prevalent variants of concern of SARS-CoV-2 is Omicron (B.1.1.529), which presents over 30 amino acid mutations compared to the Wuhan strain (23, 41). We used the structure-based designed HexaPro construct of the Omicron spike (19). The 6 prolines introduced in this construct allow a much higher yield of recombination. The relative occupancy derived from HS-AFM imaging showed important differences compared to Wuhan ($S_{Omicron}^{f-,6P}$, fig. S5, and supplementary videos), with over 54 % of the population in the all *RBD* closed state, and ~ 32 % with one *RBD* open (Fig. 1C). While cryo-EM studies have reported contradictory results, several studies agree with ours (table S1) (22, 40, 42–44). The TDPs also revealed a second distinction between the Wuhan and Omicron spikes, with transitions involving more than one *RBD* being more frequent in $S_{Omicron}^{f-,6P}$ (~ 25 %) than in S_{Wuhan}^{2P} (< 9 %) (Fig. 1D). While this result may suggest

some cooperativity in the Omicron *RBD* opening and closing, the state density histogram was still perfectly fitted with a binomial distribution, which speaks up for independent conformational changes. Additionally, global fit analysis of dwell time histograms revealed an opening rate approximately twice slower than for Wuhan spike and a slightly faster closing rate (Table 1). Our results in the Wuhan variants suggested no significant differences in *RBD* dynamics due to the *2P* substitution. Thus, the dynamics of the Omicron *S* trimers were likely not affected by the *6P* substitution, in line with the preserved immunogenicity of this construct (19). Therefore, our observed difference in *RBD* state occupancy and dynamics between Omicron and Wuhan variants is likely due to the acquired mutations during SARS-CoV-2 evolution in the human population, as recently suggested by molecular dynamics simulations (45). Moreover, the higher population of closed states in Omicron would explain the lower multivalent binding to *ACE2*, as recently described (17).

Table 1. Kinetic and thermodynamic parameters for the opening and closing transitions of an individual *RBD* within the *S* trimer. The closing equilibrium constant, K_C , was calculated from three different approaches. First, from the ratio of total number of *RBDs* observed in the closed conformation ($\Sigma RBD_{closed} = \sum_i (3-i) \times S_i$) over the total number of *RBDs* observed in the open state ($\Sigma RBD_{open} = \sum_i i \times S_i$). Second, from the probability for an *RBD* to be in the open state, as obtained from the fit of the binomial distribution $S_i = \frac{3!}{i!(3-i)!} \times p_{open}^i \times (1 - p_{open})^{3-i}$ to the relative occupancy histograms (Fig. 1C). Third, from the ratio between the closing and opening rates extracted from the global fits to the dwell time distributions (Fig. 1E).

<i>S</i> variant	$K_c \equiv \frac{\Sigma RBD_{closed}}{\Sigma RBD_{open}}$	p_{open}	$K_C \equiv \frac{1}{p_{open}} - 1$	k_c (s ⁻¹)	k_o (s ⁻¹)	$K_C \equiv \frac{k_c}{k_o}$
S_{Wuhan}^{f-}	2.6 ± 0.6	0.28 ± 0.04	2.5 ± 0.4	1.00 ± 0.28	0.40 ± 0.11	2.5 ± 1.4
S_{Wuhan}^{2P}	3.3 ± 0.8	0.26 ± 0.04	2.9 ± 0.6	0.88 ± 0.36	0.52 ± 0.21	1.7 ± 1.4
$S_{Wuhan}^{f-,2C}$	10.5 ± 2.0	0.09 ± 0.00	10.4 ± 0.0	1.81 ± 0.60	0.44 ± 0.15	4.2 ± 2.8
$S_{Omicron}^{f-,6P}$	4.0 ± 0.6	0.18 ± 0.01	4.6 ± 0.4	1.12 ± 0.26	0.21 ± 0.05	5.2 ± 2.5

Binding strength and affinity to *ACE2*

To quantify the possible effect of opening and closing of *RBD* on its binding to *ACE2*, we compared the complexation of *ACE2* to isolated *RBD* and to the S_{Wuhan}^{f-} and S_{Wuhan}^{2P} trimers using biolayer interferometry (BLI) (Fig. 2). We analyzed the time traces using a simple 1:1 binding model. The results showed similar dissociation rate constants of $3-4 \times 10^{-3}$ s⁻¹ (Table 2) for both an isolated *RBD* and a *RBD* in an *S* trimer. Conversely, *ACE2* showed a ~3-fold lower association rate constant for *RBD* within S_{Wuhan}^{f-} and S_{Wuhan}^{2P} than for isolated *RBD* (Table 2, note that in the former case, we consider *apparent* association rate constants because the conformational change kinetics may modulate association). Therefore, *RBDs* within *S* trimers showed a 3-fold higher apparent equilibrium dissociation constant (K_D^{app}) than isolated *RBDs* (Table 2).

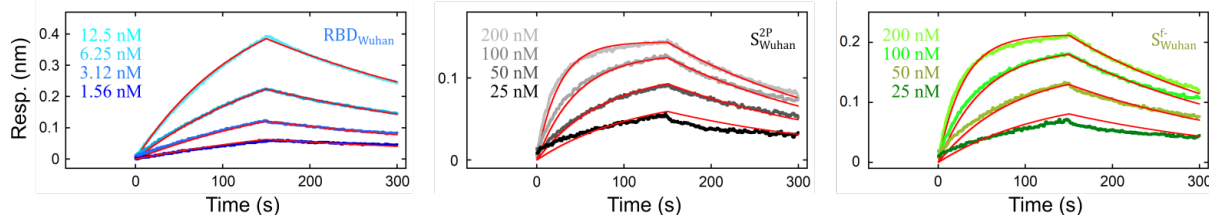


Fig. 2. Ensemble measurements of the kinetic and thermodynamic parameters for ACE2 binding to the RBD, either isolated or embedded within the S trimer. Bilayer interferometry response signals were obtained after injection of ACE2 at the indicated concentrations (from 0 to 150 s) and subsequent washing with buffer (from 150 to 300 s) for surfaces coated with either RBD_{Wuhan} (blue to cyan), S^{2P}_{Wuhan} (black to grey), or S^{f-}_{Wuhan} (green to lime). Red lines were fitted using a simple 1:1 binding model (see Table 2 for results).

Table 2. Kinetic and thermodynamic parameters for ACE2 binding to the RBD, either isolated or embedded within the S trimer. k_D and k_A respectively correspond to the dissociation and association rate constants, K_D to the k_D/k_A dissociation equilibrium constant. Whereas all three parameters refer to microscopic events in the RBD case, they refer to a phenomenological 1:1 model in the S trimer (“app” = apparent). K_C is the RBD closing equilibrium constant that can be deduced from the measured dissociation equilibrium constants thanks to the conformational selection model (see below). BLI experiments (Fig. 2) were performed at room temperature in PBS; MT experiments at constant force (Fig. 4) were performed at 30 °C in 10 mM Na-HEPES pH 7.4, 150 mM NaCl, 0.1 % Tween 20, and 0.5 mg/mL BSA.

Setup	Viral partner	k_D (10^{-3} s^{-1})	k_A (or k_A^{app} for S) ($10^5 \text{ M}^{-1}\text{s}^{-1}$)	K_D (or K_D^{app} for S) (nM)	$K_C \equiv \frac{K_D^{app}}{K_D} - 1$
BLI	RBD_{Wuhan}	3.0 ± 0.0	3.8 ± 0.0	7.8 ± 0.1	
	S^{2P}_{Wuhan}	4.3 ± 0.0	1.7 ± 0.0	24.5 ± 0.3	2.1 ± 0.1
	S^{f-}_{Wuhan}	4.1 ± 0.0	1.5 ± 0.0	26.9 ± 0.3	2.5 ± 0.1
MT	RBD_{Wuhan}	21.3 ± 1.4	9.0 ± 1.5	23.7 ± 3.6	
	S^{2P}_{Wuhan}	30.1 ± 2.3	3.6 ± 0.5	83.5 ± 10.7	2.5 ± 0.5

BLI measurements were made with minor mechanical stress applied to the analytes. However, during normal breathing and even more during pathological coughing, the airflow in the respiratory tract applies important viscous drag forces to virus particles, affecting the interaction of the S trimers with ACE2 (3, 10, 14, 23). Recent single-molecule force spectroscopy (SMFS) probed the forces required to rupture RBD and S trimer/ACE2 complexes, proposing force-tuned avidity (17). Various SMFS reports have compared for different SARS-CoV-2 variants the influence of force on the stability of the complexes formed by ACE2 with both the RBD or an S trimer (11, 12, 15). However, they have only explored a restricted range of loading rates whereas under physiological conditions, the shear rate applied by the airflow varies over 7 orders of magnitude (46). Hence, we conducted HS-FS to measure the rupture forces of RBD and S trimers in complex with ACE2, over 5 decades of force loading rates (Fig. 3A-C) (47, 48). To covalently immobilize the molecules to the surfaces, we engineered RBD, S trimers, and ACE2 with a C-terminal ybbR tag (Fig. 3A) (49). This strategy enables site-directed grafting through a 32-nm polyethylene glycol flexible linker that allows the molecules to freely align with the pulling vectors. Isolated RBD and S trimers unbinding from ACE2 showed similar rupture forces over the investigated range (Fig. 3C). The most probable rupture forces first increased linearly with the logarithm of the loading rate and showed an upturn at the highest values (Fig. 3C, see Materials

and Methods). The free energy landscape parameters obtained from fitting the force spectra with the Cossio-Hummer-Szabo (CHS) model were similar: intrinsic dissociation rate $k_D \sim 10^{-2} \text{ s}^{-1}$, distance to transition state $x^\ddagger \sim 0.9 \text{ nm}$, and barrier height $\Delta G^\ddagger \sim 15 \text{ k}_\text{B}T$ (Fig. 3C, table S3) (50). This observation confirmed that the binding strength and dissociation rates are parameters characteristic of the *RBD* and are not importantly affected by their inclusion within the *S* trimer.

The dissociation at slow shear rates or low forces is also important for viral infection (16). While HS-FS covers a wide range of loading rates, it has a limited force sensitivity ($\gtrsim 10 \text{ pN}$). Thus, to access lower forces, we employed MT (51) with the same ybbR constructs engrafted on modular junctured-DNA (J-DNA) scaffolds (Fig. 3D) (52). This procedure enabled the repeated probing of the dissociation of single RBD_{Wuhan} or $S_{Wuhan}^{2P}/ACE2$ complexes at forces as low as $\sim 1 \text{ pN}$. The histogram of dwell time in the looped conformation (bound complex) at each applied force followed an exponential distribution with characteristic time τ_L^F (Fig. 3E). By averaging τ_L^F across different J-DNA scaffolds and correlating it to the dissociation rate constant under force, we characterized the energy landscape by fitting the Bell model (53) (Fig. 3F). We obtained in this manner $k_D \sim (23 \pm 2) \times 10^{-3} \text{ s}^{-1}$ and $x^\ddagger \sim 0.8 \text{ nm}$ for RBD_{Wuhan} and S_{Wuhan}^{2P} (Fig. 3F, table S3), in fair agreement with the values derived from HS-FS experiments. Additionally, the k_D values obtained at different temperatures and fitted with the Arrhenius equation led to activation energies E_D , that were similar for RBD_{Wuhan} and S_{Wuhan}^{2P} (Fig. 3G, table S3), again confirming that the dissociation pathway is not impacted by the integration of the *RBD* within *S* trimers, as suggested by previous SMFS data (see supplementary text S2) (11–13, 15–17, 54).

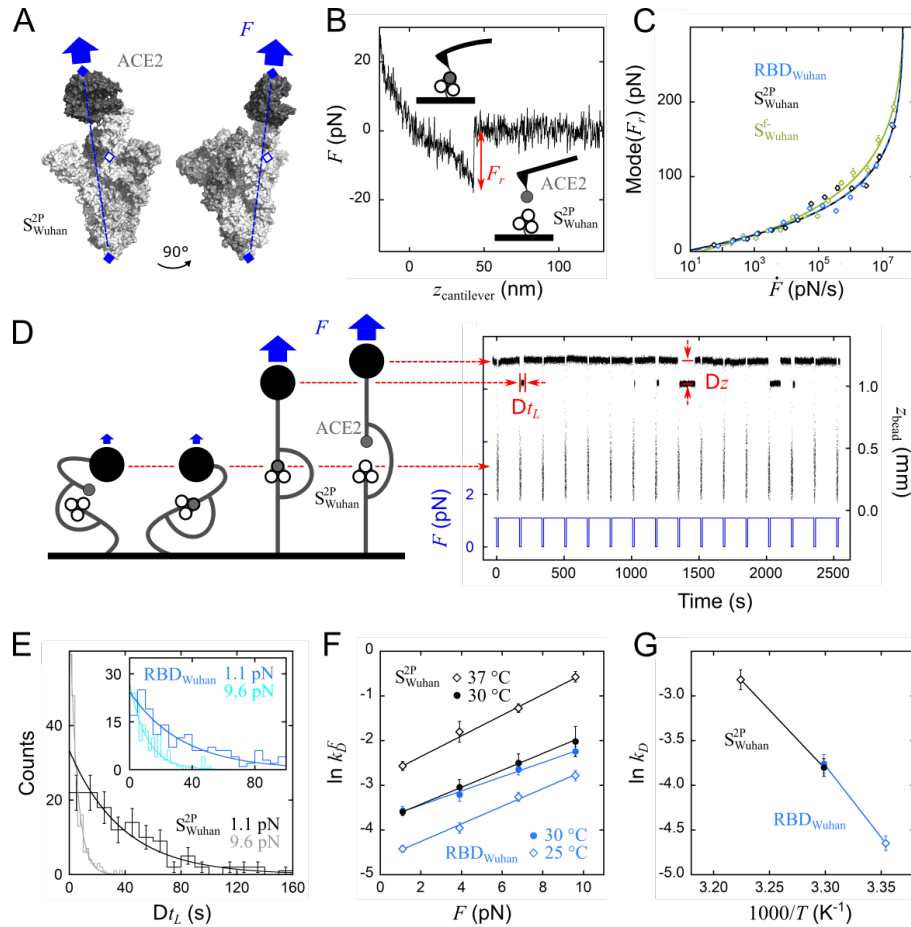


Fig. 3. Single-molecule measurements of the dissociation kinetics and force response for ACE2 bound to the RBD, either isolated or embedded within the S trimer. (A) Cryo-EM structure of the complex $S_{\text{Wuhan}}^{2\text{P}}$ /ACE2 with one RBD open and bound (PDB 7A94 (7) visualized with PyMOL). The pulling direction (blue dashed line) connects the positions of the ybbR tags (full diamonds) used to tether S and ACE2. The open diamond is the position of the ybbR tag when pulling on isolated RBD. (B) Example of HS-AFM force-distance curve recorded on a $S_{\text{Wuhan}}^{2\text{P}}$ /ACE2 complex and showing how the rupture force, F_r , is determined. (C) Dynamic force spectra from HS-AFM for ACE2 unbinding from RBD_{Wuhan} , $S_{\text{Wuhan}}^{2\text{P}}$, and S_{Wuhan}^{f-} (blue, black, and kaki, respectively). The most probable rupture force was determined as the mode of the F_r distribution at each loading rate, \dot{F} (figs. S6-S8; error bars are SEM). Fits to the CHS model (Eqs. 1-2 in Materials and Methods) provided the position of the transition states in energy and space, ΔG^\ddagger and x^\ddagger , as well as the dissociation rate constants at zero force, k_D (table S3). (D) Force-cycling procedure applied with MT to $S_{\text{Wuhan}}^{2\text{P}}$ and ACE2 engrafted on J-DNA. At near 0 pN, the scaffold extension is low (two leftmost schemes, not to scale); the scaffold tips can encounter each other, and the two proteins can associate. When the force is increased to a value F , the bead pulls on the looped J-DNA and the extension reaches a higher value (middle scheme). Eventually, the two partners spontaneously separate and the extension increases again (right scheme). Upon repeating the force variation multiple times, one obtains a time-trace on which dissociation events are characterized by their dwell time in the looped conformation, Δt_L , and the amplitude of their extension jump, Δz . (E) Examples of Δt_L histograms collected on $S_{\text{Wuhan}}^{2\text{P}}$ /ACE2 at $F = 1.1$ and 9.6 pN, $T = 30$ °C (black and grey, respectively; $N = 101$ and 136 rupture events after exclusion of the first bin; Poissonian counting error bars only shown at 1.1 pN for the sake of clarity). Data were fitted by single-exponential distributions to yield characteristic times, τ_L^F , equal to 38.3 ± 5.4 and 5.16 ± 0.57 s (\pm SE). Inset, same plots for a RBD_{Wuhan} /ACE2 complex (blue and cyan, respectively; $N = 150$ and 138) leading to $\tau_L^F = 33.9 \pm 4.5$ and 11.3 ± 1.3 s. (F) Force-dependence for the dissociation rate constant, $\ln k_D^F = 1/\tau_L^F$, measured on RBD_{Wuhan} /ACE2 (blue), and $S_{\text{Wuhan}}^{2\text{P}}$ /ACE2 (black) at various temperatures. Data were fitted to the Bell model (Eq. 3 in Materials and Methods) to provide the dissociation rate constant at zero-force, k_D , and the

distance to the transition state, x^\ddagger (table S3). **(G)** Temperature-dependence of k_D for RBD_{Wuhan} (blue) and S_{Wuhan}^{2P} (black). Data were fitted to the Arrhenius equation (Eq. 4) to yield the activation energies, E_D (table S3).

We then estimated the association kinetics by measuring the adhesion probability P at different contact times between an AFM tip functionalized with *ACE2* and a surface coated with the *RBD* or the *S* trimer (Fig. 4A) (55, 56). *S* trimers appeared ~2 to 4 times slower to bind to *ACE2* (0.17-0.33 s) than isolated *RBD* (0.08 s). However, the interpretation of these results requires too many hypotheses on the behavior of the system at the molecular scale, which consequently makes the extraction of quantitative data difficult (supplementary text S3). Therefore, to accurately quantify binding, we monitored the looping and unlooping of J-DNA scaffolds at very low, constant force (0.1 pN) while increasing concentrations of *ACE2* in solution (Fig. 4B-C). As expected, the dwell times in the looped conformation, Δt_L , obeyed monoexponential distributions with characteristic times $\tau_L^{F \approx 0}$ that did not depend on the *ACE2* concentration and were similar for RBD_{Wuhan} and S_{Wuhan}^{2P} (Fig. 4D, F). It yielded k_D values (Fig. 4G, Table 2) in fair agreement with those derived above from MT-based SMFS experiments (table S3). In contrast, monoexponential fits to the histograms of the dwell times in the unlooped conformation, Δt_U , provided characteristic times $\tau_U^{F \approx 0}$ that increased with the *ACE2* concentration – indicating that the formation of a complex between the two scaffolded components becomes more difficult as more *ACE2* molecules from the solution occupy the *RBDs* (Fig. 4E-F). To be more quantitative, we studied the linear variation, as a function of *ACE2* concentration, of the ratio between the time spent in the unlooped and in the looped conformation (57). In this way, we obtained the dissociation equilibrium constants for the complex of *ACE2* with RBD_{Wuhan} and with S_{Wuhan}^{2P} (Fig. 4H and Eqs. 5-6 in Materials and Methods): an *RBD* within the *S* trimer showed a ~3.5-fold lower affinity than an isolated *RBD* (Fig. 4I, Table 2), which corroborates the BLI measurements (Fig. 2, Table 2). Considering the dissociation rate constant values, it translated into an association rate constant for an isolated *RBD* that is ~2.5-fold higher than for an *RBD* within the *S* trimer.

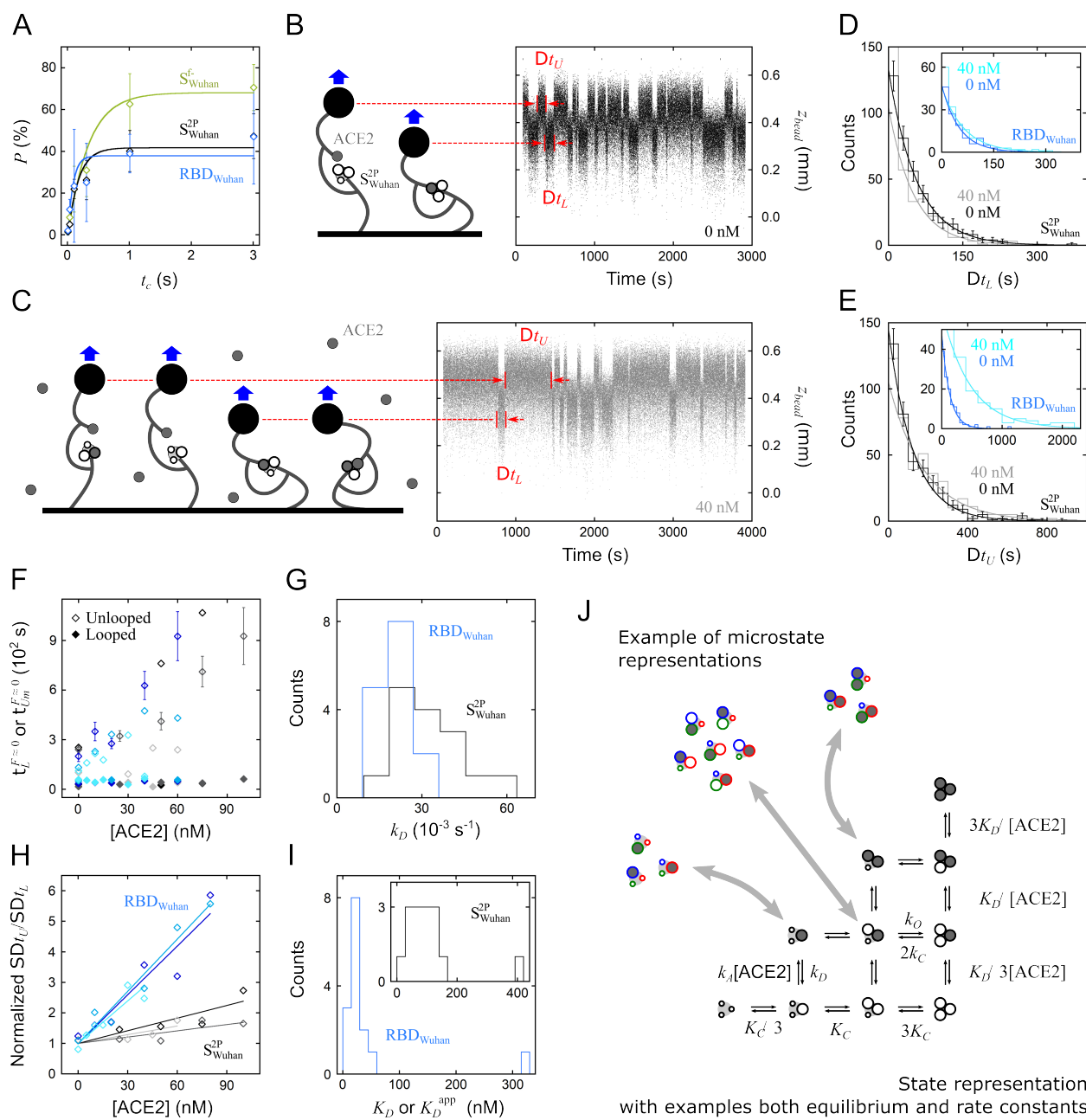
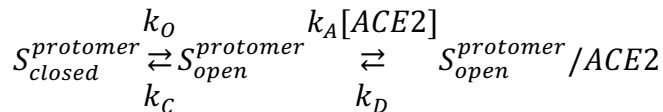


Fig. 4. Single-molecule measurements of the kinetic and thermodynamic parameters for ACE2 binding to the RBD, either isolated or embedded within the S trimer. (A) Adhesion probability, P , as a function of the contact time, t_c , between the AFM cantilever functionalized with ACE2 and the surface coated with either RBD_{Wuhan} , S^{2P}_{Wuhan} , or S^{f-}_{Wuhan} (blue, black, and kaki, respectively). Error bars correspond to SEM. Fits to the first-order kinetics provided the characteristic interaction time ($\tau_U = 0.08 \pm 0.04$ s for RBD_{Wuhan} , 0.33 ± 0.13 s for S^{f-}_{Wuhan} , and 0.17 ± 0.06 s for S^{2P}_{Wuhan}). (B, C) Representative time traces obtained during the titration by soluble ACE2 of J-DNA grafted with ACE2 and S^{2P}_{Wuhan} , ACE2 being absent or present in solution at 40 nM. The applied constant force of 0.1 pN was low enough for the proteins on the scaffold to spontaneously dissociate and associate in *cis*; it was also high enough for the looped and unlooped conformations to be distinguished, and the corresponding dwell times, respectively Δt_L and Δt_U , to be measured. (D) Examples of Δt_L histograms collected on a S^{2P}_{Wuhan} /ACE2 complex and fitted by single-exponential distributions to yield characteristic times for the looped conformation, $\tau_L^{F=0}$, equal to 57.0 ± 4.4 and 50.9 ± 4.3 s (\pm SE) for $[ACE2] = 0$ and 40 nM (resp. black and grey, $N = 262$ and 187 rupture events). Inset, same plots obtained on a RBD_{Wuhan} /ACE2 complex, with $\tau_L^{F=0} = 50.7 \pm 7.1$ and 64.0 ± 8.0 s for $[ACE2] = 0$ and 40 nM (resp. blue and cyan, $N = 83$ and 109). (E) Examples of Δt_U histograms collected on the same complex. For

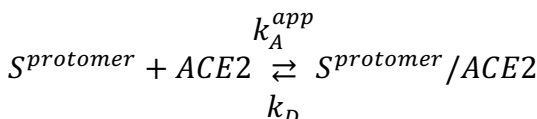
$S_{Wuhan}^{2P}/ACE2$, it gave characteristic times for the unlooped conformation $\tau_{Um}^{F\approx 0} = 124.6 \pm 8.3$ and 180.2 ± 12.6 s for $[ACE2] = 0$ and 40 nM (resp. black and grey, $N = 256$ and 300). For $RBD_{Wuhan}/ACE2$ (inset) we obtain $\tau_{Um}^{F\approx 0} = 132.5 \pm 16.8$ and 474.4 ± 66.0 s for $[ACE2] = 0$ and 40 nM (resp. blue and cyan, $N = 90$ and 98). **(F)** Variation, as a function of titrant concentration $[ACE2]$, of $\tau_l^{F\approx 0}$ (full markers) and $\tau_{Um}^{F\approx 0}$ (open markers). Data are given for three representative scaffolds grafted with $ACE2$ and RBD_{Wuhan} (blue to cyan) and three others with $ACE2$ and S_{Wuhan}^{2P} (black to grey). Each data point was obtained by monitoring a total of $N = 58$ to 310 events; error bars correspond to SE and, for clarity, they are only displayed for two examples. **(G)** Distributions of the dissociation rate constants obtained on individual scaffolds for $RBD_{Wuhan}/ACE2$ and for $S_{Wuhan}^{2P}/ACE2$ (resp. blue and black, 15 and 15 J-DNA, $N = 73$ to 764 dissociation events pooled per scaffold over the whole concentration range; Table 2). **(H)** Variation, as a function of the concentration in titrant, of the ratio between the total time spent in the unlooped conformation and the total time spent in the looped one. Linear fits with Eqs. 5-6 resulted in $K_D = 17.5 \pm 1.1$, 18.8 ± 1.9 , and 21.5 ± 2.7 nM for the three exemplary scaffolds grafted with $ACE2$ and RBD_{Wuhan} (blue to cyan) and in $K_D^{app} = 72.3 \pm 10.9$, 104.8 ± 24.1 , and 145.3 ± 28.7 nM for the three other ones with $ACE2$ and S_{Wuhan}^{2P} (black to grey). For each scaffold, both the data points and the fit have been renormalized by the fit value at $[ACE2] = 0$ nM, making it easier to visualize the dissociation equilibrium constant as the inverse of a slope (fig. S9 for the non-normalized data). **(I)** Distributions of the dissociation equilibrium constants obtained on individual scaffolds for $RBD_{Wuhan}/ACE2$ (blue, 15 J-DNA) and for $S_{Wuhan}^{2P}/ACE2$ (inset, black, 15 J-DNA; Table 2). **(J)** Schematic description of all possible states for the S trimer and for its complexes with either one, two, or three $ACE2$ molecules, as well as of all possible transitions. The microstates are only represented for 3 states and similarly, the equilibrium and rate constants are only explicated for a subset of the reactions. K_D is the dissociation equilibrium constant of the $RBD/ACE2$ complex and k_A and k_D the corresponding association, and dissociation rate constants, respectively.

Conformational selection model

All our experimental datasets, drawn from different experiments and methods, are coherent and converge towards a single model. Our results show that each S protomer ($S^{protomer}$) acts independently and can either be open ($S_{open}^{protomer}$) or closed ($S_{closed}^{protomer}$), and associate to $ACE2$ according to the reaction network of Fig. 4J. To account for that, we propose a conformational selection model describing a serial, two-step mechanism. First, the S protomer in the trimer opens and, second, it binds to $ACE2$:



From the experimental point of view, it appears as a single-step process because the relaxation time characterizing the RBD conformational transition $(k_o + k_c)^{-1} \sim 0.7$ s is much shorter than the time characterizing the binding-unbinding of $ACE2$ on the open RBD $(k_A[ACE2] + k_d)^{-1} \gtrsim 13$ s over the whole used concentration range (Tables 1 and 2). Therefore, the first step is always at equilibrium with respect to the second and this conformational selection scheme simplifies into:



Since in the S trimer, each RBD has a probability p_{open} to be accessible to $ACE2$, it yields an apparent equilibrium dissociation constant $K_D^{app} = K_D/p_{open} = K_D(1 + K_c)$ and, assuming unaffected dissociation rates, an apparent association rate $k_A^{app} = k_A p_{open} = k_A/(1 + K_c)$ (supplementary text S4) (58, 59). Therefore, if the RBD opening probability is high, or the opening rate is much faster than the closing rate, $K_D^{app} \rightarrow K_D$, not affecting the binding. In contrast, if the RBD opening probability tends to zero, or opening is much slower than closing, $K_D^{app} \rightarrow \infty$, suppressing the binding. Importantly, because the binding is only modulated by K_c , it does not

depend on the *RBD* valency in the *S* trimer, making the model applicable to both trimers and protomers. The experimental *RBD* opening/closing rates presented in Table 1 resulted in $K_C \sim 2$ for the S_{Wuhan}^{f-} and S_{Wuhan}^{2P} trimers, leading to $K_D^{app} = 3K_D$, which quantitatively explains the values derived from K_D^{app} and K_D in both the BLI (ensemble) and MT (single-molecule) measurements presented in Table 2.

From these results, it appears that modulating the rapid opening and closing of the *RBD* tunes the affinity of the whole spike. This concept should be further evidenced with the $S_{Wuhan}^{f-,2C}$ mutant in which a disulfide bond has been artificially inserted to impede opening. Indeed, according to the K_C obtained from HS-AFM imaging, this modulation should lead to an affinity to *ACE2* up to 11 times lower than the one of S_{Wuhan}^{f-} . Previous structural and BLI works on similar *S* trimers mutant locked in the closed conformation are in agreement with our results (24).

Previous works showed that for the Omicron variant, the isolated *RBD* and the *S* trimer have a significantly higher binding affinity for *ACE2* compared to the Wuhan variant, but some reports indicate all *RBD* in the closed state, which should result in a lower binding affinity (23, 41, 60). From our K_C values, we estimated a ~6-fold reduction in *ACE2* binding affinity for a *RBD* within the Omicron spike trimer compared to an isolated *RBD*. In theory, the higher probability for the Omicron spike to have all *RBD* in the closed state compared to the Wuhan spike should prevent infection. However, this is compensated by mutations in the *RBD* which enable it to complex *ACE2* with higher affinity (23, 41, 44, 61). The advantage of this apparently neutral deal would be that an Omicron spike with lower probability of presenting *RBD* open is less susceptible to be neutralized by antibodies binding to the *RBD*. Therefore, our results partly explain the high immune evasion of the Omicron spike (45, 62).

Despite the enormous research effort undertaken since the emergence of COVID-19, the dynamics and functional mechanisms whereby SARS-CoV-2 enter their host have been challenging to explain. By combining molecular engineering with the ensemble and single-molecule techniques, we unveiled the multistep molecular mechanisms of the *S* trimer binding to *ACE2*. Our results show independence between conformations of the three protomers in the spike and a faster relaxation for the *RBD* opening and closing reaction than for *ACE2* association and dissociation. We thus propose a conformational selection model in which the *RBD* open/close transition modulates the binding to *ACE2*, independently of the number of accessible binding sites and binding affinity. This model is especially significant for the Omicron variant, which presents an increased *RBD* closing equilibrium constant through mutations away from the receptor binding motif together with an increased *RBD/ACE2* binding affinity constant (41). This would lead to a powerful mechanism to evade neutralizing antibodies that recognize the open *RBD*, while still binding to the host. Therefore, our results help explain the observed enhanced infectivity of Omicron and potentially of other SARS-CoV-2 variants of concern. Finally, the analysis of *RBD* opening and closing developed for HS-AFM imaging is adaptable to other techniques, such as cryo-EM or smFRET. We therefore provide a tool to predict the modulation of spike affinity by conformational changes and to test possible cooperative effects between protomers. Although not restricted to, we anticipate this approach to be useful for the study of other viral systems, *e.g.* future SARS-CoV-2 emerging variants and other human- or animal-borne coronaviruses (63). Furthermore, the experimental and conceptual framework we have developed should help in the conception of more effective vaccines and antibodies.

Acknowledgements:

We thank M. Backovic (UVS, Institut Pasteur, Paris) for logistics; M. A. Nash (Chemistry Dept., Univ. of Basel) for the gift of the sfp plasmid; P. England and the Biophysics Facility (Institut Pasteur) for access to the BLI; D. Joshi (RCAS, Academia Sinica, Taipei) for advises on PyMOL; P.-H. Puech and L. Limozin (LAI, Aix-Marseille Univ.) for insightful discussions; and J. Reguera (AFMB, Aix-Marseille Univ.) for critical reading of the manuscript.

Funding:

This project has received funding from the Human Frontier Science Program (HFSP, grant No. RGP0056/2018 to FR), the European Research Council (ERC) under the European Union's Horizon 2020 research and innovation program (grant agreement No 772257 to FR), the European Union's Horizon 2020 research and innovation program (Marie Skłodowska-Curie grant No. 895819 to CV), the Turing Centre for Living Systems (Centuri), PSL-Valorisation (grant J-DNA 2 to CG and TS), Labex IBEID (grant ANR-10-LABX-62-IBEID to FAR), and the Pasteur Coronavirus Task-Force (grants Allospike and TooLab to FAR). The Molecular Motors and Machines team at IBENS has received a "Coup d'élan" from the Fondation Bettencourt Schueller and is also an "Equipe labellisée" by the Ligue Nationale Contre le Cancer. FSt benefited from a doctoral fellowship from the Ministère de l'Enseignement Supérieur et de la Recherche. The project leading to this publication has received funding from France 2030, the French Government program managed by the French National Research Agency (ANR-16-CONV-0001), and from Excellence Initiative of Aix-Marseille University - A*MIDEX.

Author contributions:

CG, TS, FAR, and FR supervised research. IF, AM, EB, and AS designed and produced the *ACE2*, *RBD*, and spike proteins. PS and FSu acquired the HS-AFM videos. PS and TB developed and applied the ImageJ macros to extract the conformational trajectories from HS-AFM videos. FR analyzed conformational trajectories. CG and FR developed the conformational selection model and implemented it for data analysis. IF, EB and PGC conducted BLI measurements. CV performed the AFM and HS-AFM SMFS experiments and analyzed data with FR. DK synthesized J-DNA and coupled them to the molecular partners. DK and JP realized MT measurements. FSt developed the software for analyzing the constant-force MT experiments. PS, CG, CV, and FR wrote the paper with the contributions of all the authors.

Competing interests: PSL valorization has submitted a patent related to the J-DNA forceps (PCT FR2018/053533) with DK, TS and CG among the inventors.

Data and materials availability: All the materials and methods are detailed in the *Supplementary Materials*, including statistics. The code used for image processing is available on the GitHub repository (source code: <https://github.com/centuri-engineering/ProtruDe/>). Representative HS-AFM videos are provided in the *Supplementary Materials*. The raw data are available on request from the authors.

Supplementary Materials

This PDF file includes: Materials and Methods, Supplementary Text S1 to S4, Figs. S1 to S9, Tables S1 to S3, Supplementary Videos (SV) information, References

Videos SV1 to SV20

References:

1. R. Yan, Y. Zhang, Y. Li, L. Xia, Y. Guo, Q. Zhou, Structural basis for the recognition of SARS-CoV-2 by full-length human ACE2. *Science* **367**, 1444–1448 (2020).
2. A. C. Walls, Y.-J. Park, M. A. Tortorici, A. Wall, A. T. McGuire, D. Veesler, Structure, function, and antigenicity of the SARS-CoV-2 spike glycoprotein. *Cell* **181**, 281-292.e6 (2020).
3. D. Wrapp, N. Wang, K. S. Corbett, J. A. Goldsmith, C.-L. Hsieh, O. Abiona, B. S. Graham, J. S. McLellan, Cryo-EM structure of the 2019-nCoV spike in the prefusion conformation. *Science* **367**, 1260–1263 (2020).
4. Y. Cai, J. Zhang, T. Xiao, H. Peng, S. M. Sterling, R. M. Walsh, S. Rawson, S. Rits-Volloch, B. Chen, Distinct conformational states of SARS-CoV-2 spike protein. *Science* **369**, 1586–1592 (2020).
5. R. Henderson, R. J. Edwards, K. Mansouri, K. Janowska, V. Stalls, S. M. C. Gobéil, M. Kopp, D. Li, R. Parks, A. L. Hsu, M. J. Borgnia, B. F. Haynes, P. Acharya, Controlling the SARS-CoV-2 spike glycoprotein conformation. *Nat. Struct. Mol. Biol.* **27**, 925–933 (2020).
6. H. Yao, Y. Song, Y. Chen, N. Wu, J. Xu, C. Sun, J. Zhang, T. Weng, Z. Zhang, Z. Wu, L. Cheng, D. Shi, X. Lu, J. Lei, M. Crispin, Y. Shi, L. Li, S. Li, Molecular architecture of the SARS-CoV-2 virus. *Cell* **183**, 730-738.e13 (2020).
7. D. J. Benton, A. G. Wrobel, P. Xu, C. Roustan, S. R. Martin, P. B. Rosenthal, J. J. Skehel, S. J. Gamblin, Receptor binding and priming of the spike protein of SARS-CoV-2 for membrane fusion. *Nature* **588**, 327–330 (2020).
8. Z. Ke, J. Oton, K. Qu, M. Cortese, V. Zila, L. McKeane, T. Nakane, J. Zivanov, C. J. Neufeldt, B. Cerikan, J. M. Lu, J. Peukes, X. Xiong, H.-G. Kräusslich, S. H. W. Scheres, R. Bartenschlager, J. A. G. Briggs, Structures and distributions of SARS-CoV-2 spike proteins on intact virions. *Nature* **588**, 498–502 (2020).
9. C. Xu, Y. Wang, C. Liu, C. Zhang, W. Han, X. Hong, Y. Wang, Q. Hong, S. Wang, Q. Zhao, Y. Wang, Y. Yang, K. Chen, W. Zheng, L. Kong, F. Wang, Q. Zuo, Z. Huang, Y. Cong, Conformational dynamics of SARS-CoV-2 trimeric spike glycoprotein in complex with receptor ACE2 revealed by cryo-EM. *Sci. Adv.* **7**, eabe5575 (2021).
10. P. Zhou, X.-L. Yang, X.-G. Wang, B. Hu, L. Zhang, W. Zhang, H.-R. Si, Y. Zhu, B. Li, C.-L. Huang, H.-D. Chen, J. Chen, Y. Luo, H. Guo, R.-D. Jiang, M.-Q. Liu, Y. Chen, X.-R. Shen, X. Wang, X.-S. Zheng, K. Zhao, Q.-J. Chen, F. Deng, L.-L. Liu, B. Yan, F.-X. Zhan, Y.-Y. Wang, G.-F. Xiao, Z.-L. Shi, A pneumonia outbreak associated with a new coronavirus of probable bat origin. *Nature* **579**, 270–273 (2020).
11. J. Yang, S. J. L. Petitjean, M. Koehler, Q. Zhang, A. C. Dumitru, W. Chen, S. Derclaye, S. P. Vincent, P. Soumillion, D. Alsteens, Molecular interaction and inhibition of SARS-CoV-2 binding to the ACE2 receptor. *Nat. Commun.* **11**, 4541 (2020).
12. W. Cao, C. Dong, S. Kim, D. Hou, W. Tai, L. Du, W. Im, X. F. Zhang, Biomechanical characterization of SARS-CoV-2 spike RBD and human ACE2 protein-protein interaction. *Biophys. J.* **120**, 1011–1019 (2021).
13. F. Tian, B. Tong, L. Sun, S. Shi, B. Zheng, Z. Wang, X. Dong, P. Zheng, N501Y mutation of spike protein in SARS-CoV-2 strengthens its binding to receptor ACE2. *eLife* **10**, e69091 (2021).
14. W. Hu, Y. Zhang, P. Fei, T. Zhang, D. Yao, Y. Gao, J. Liu, H. Chen, Q. Lu, T. Mudianto, X. Zhang, C. Xiao, Y. Ye, Q. Sun, J. Zhang, Q. Xie, P.-H. Wang, J. Wang, Z. Li, J. Lou, W. Chen, Mechanical activation of spike fosters SARS-CoV-2 viral infection. *Cell Res.* **31**, 1047–1060 (2021).
15. M. Koehler, A. Ray, R. A. Moreira, B. Juniku, A. B. Poma, D. Alsteens, Molecular insights into receptor binding energetics and neutralization of SARS-CoV-2 variants. *Nat. Commun.* **12**, 6977 (2021).
16. M. S. Bauer, S. Gruber, A. Hausch, P. S. F. C. Gomes, L. F. Milles, T. Nicolaus, L. C. Schendel, P. L. Navajas, E. Procko, D. Lietha, M. C. R. Melo, R. C. Bernardi, H. E. Gaub, J. Lipfert, A tethered ligand assay to probe SARS-CoV-2:ACE2 interactions. *Proc. Natl. Acad. Sci.* **119**, e2114397119 (2022).
17. R. Zhu, D. Canena, M. Sikora, M. Klausberger, H. Seferovic, A. R. Mehdipour, L. Hain, E. Laurent, V. Monteil, G. Wirnsberger, R. Wieneke, R. Tampé, N. F. Kienzl, L. Mach, A. Mirazimi, Y. J. Oh, J. M. Penninger, G.

Hummer, P. Hinterdorfer, Force-tuned avidity of spike variant-ACE2 interactions viewed on the single-molecule level. *Nat. Commun.* **13**, 7926 (2022).

- 18. J. Shang, Y. Wan, C. Luo, G. Ye, Q. Geng, A. Auerbach, F. Li, Cell entry mechanisms of SARS-CoV-2. *Proc. Natl. Acad. Sci.* **117**, 11727–11734 (2020).
- 19. C.-L. Hsieh, J. A. Goldsmith, J. M. Schaub, A. M. DiVenere, H.-C. Kuo, K. Javanmardi, K. C. Le, D. Wrapp, A. G. Lee, Y. Liu, C.-W. Chou, P. O. Byrne, C. K. Hjorth, N. V. Johnson, J. Ludes-Meyers, A. W. Nguyen, J. Park, N. Wang, D. Amengor, J. J. Lavinder, G. C. Ippolito, J. A. Maynard, I. J. Finkelstein, J. S. McLellan, Structure-based design of prefusion-stabilized SARS-CoV-2 spikes. *Science* **369**, 1501–1505 (2020).
- 20. X. Xiong, K. Qu, K. A. Ciazenska, M. Hosmillo, A. P. Carter, S. Ebrahimi, Z. Ke, S. H. W. Scheres, L. Bergamaschi, G. L. Grice, Y. Zhang, The CITIID-NIHR COVID-19 BioResource Collaboration, J. Bradley, P. A. Lyons, K. G. C. Smith, M. Toshner, A. Elmer, C. Ribeiro, J. Kourampa, S. Jose, J. Kennet, J. Rowlands, A. Meadows, C. O'Brien, R. Rastall, C. Crucusio, S. Hewitt, J. Price, J. Calder, L. Canna, A. Bucke, H. Tordesillas, J. Harris, V. Ruffolo, J. Domingo, B. Graves, H. Butcher, D. Caputo, E. Le Gresley, B. J. Dunmore, J. Martin, E. Legchenko, C. Treacy, C. Huang, J. Wood, R. Sutcliffe, J. Hodgson, J. Shih, S. Graf, Z. Tong, F. Mescia, T. Tilly, C. O'Donnell, K. Hunter, L. Pointon, N. Pond, M. Wylot, E. Jones, S. Fawke, B. Bullman, L. Bergamaschi, L. Turner, I. Jarvis, O. Omarjee, A. De Sa, J. Marsden, A. Betancourt, M. Perera, M. Epping, N. Richoz, G. Bower, R. Sharma, F. Nice, O. Huhn, H. Stark, N. Walker, K. Stirrups, N. Ovington, E. Dewhurst, E. Li, S. Papadia, J. A. Nathan, S. Baker, L. C. James, H. E. Baxendale, I. Goodfellow, R. Doffinger, J. A. G. Briggs, A thermostable, closed SARS-CoV-2 spike protein trimer. *Nat. Struct. Mol. Biol.* **27**, 934–941 (2020).
- 21. D. J. Benton, A. G. Wrobel, C. Roustan, A. Borg, P. Xu, S. R. Martin, P. B. Rosenthal, J. J. Skehel, S. J. Gamblin, The effect of the D614G substitution on the structure of the spike glycoprotein of SARS-CoV-2. *Proc. Natl. Acad. Sci.* **118**, e2022586118 (2021).
- 22. J. Zhang, Y. Cai, T. Xiao, J. Lu, H. Peng, S. M. Sterling, R. M. Walsh, S. Rits-Volloch, H. Zhu, A. N. Woosley, W. Yang, P. Sliz, B. Chen, Structural impact on SARS-CoV-2 spike protein by D614G substitution. *Science* **372**, 525–530 (2021).
- 23. W. Yin, Y. Xu, P. Xu, X. Cao, C. Wu, C. Gu, X. He, X. Wang, S. Huang, Q. Yuan, K. Wu, W. Hu, Z. Huang, J. Liu, Z. Wang, F. Jia, K. Xia, P. Liu, X. Wang, B. Song, J. Zheng, H. Jiang, X. Cheng, Y. Jiang, S.-J. Deng, H. E. Xu, Structures of the Omicron spike trimer with ACE2 and an anti-Omicron antibody. *Science* **375**, 1048–1053 (2022).
- 24. K. Qu, Q. Chen, K. A. Ciazenska, B. Liu, X. Zhang, J. Wang, Y. He, J. Guan, J. He, T. Liu, X. Zhang, A. P. Carter, X. Xiong, J. A. G. Briggs, Engineered disulfide reveals structural dynamics of locked SARS-CoV-2 spike. *PLOS Pathog.* **18**, e1010583 (2022).
- 25. M. Gur, E. Taka, S. Z. Yilmaz, C. Kilinc, U. Aktas, M. Golcuk, Conformational transition of SARS-CoV-2 spike glycoprotein between its closed and open states. *J. Chem. Phys.* **153**, 075101 (2020).
- 26. B. Turoňová, M. Sikora, C. Schürmann, W. J. H. Hagen, S. Welsch, F. E. C. Blanc, S. Von Bülow, M. Gecht, K. Bagola, C. Hörner, G. Van Zandbergen, J. Landry, N. T. D. De Azevedo, S. Mosalaganti, A. Schwarz, R. Covino, M. D. Mühlbach, G. Hummer, J. Krijnse Locker, M. Beck, In situ structural analysis of SARS-CoV-2 spike reveals flexibility mediated by three hinges. *Science* **370**, 203–208 (2020).
- 27. M. I. Zimmerman, G. Bowman, SARS-CoV-2 Simulations go exascale to capture spike opening and reveal cryptic pockets across the proteome. *Biophys. J.* **120**, 651–659 (2021).
- 28. Y. K. Choi, Y. Cao, M. Frank, H. Woo, S.-J. Park, M. S. Yeom, T. I. Croll, C. Seok, W. Im, Structure, dynamics, receptor binding, and antibody binding of the fully glycosylated full-length SARS-CoV-2 spike protein in a viral membrane. *J. Chem. Theory Comput.* **17**, 2479–2487 (2021).
- 29. M. Lu, P. D. Uchil, W. Li, D. Zheng, D. S. Terry, J. Gorman, W. Shi, B. Zhang, T. Zhou, S. Ding, R. Gasser, J. Prévost, G. Beaudoin-Bussières, S. P. Anand, A. Laumaea, J. R. Grover, L. Liu, D. D. Ho, J. R. Mascola, A. Finzi, P. D. Kwong, S. C. Blanchard, W. Mothes, Real-time conformational dynamics of SARS-CoV-2 spikes on virus particles. *Cell Host Microbe* **28**, 880-891.e8 (2020).
- 30. V. H. B. Serrão, J. E. Lee, FRETing over SARS-CoV-2: conformational dynamics of the spike glycoprotein. *Cell Host Microbe* **28**, 778–779 (2020).

31. Z. Yang, Y. Han, S. Ding, W. Shi, T. Zhou, A. Finzi, P. D. Kwong, W. Mothes, M. Lu, SARS-CoV-2 variants increase kinetic stability of open spike conformations as an evolutionary strategy. *mBio* **13**, e03227-21 (2022).
32. M. A. Díaz-Salinas, Q. Li, M. Ejemel, L. Yurkovetskiy, J. Luban, K. Shen, Y. Wang, J. B. Munro, Conformational dynamics and allosteric modulation of the SARS-CoV-2 spike. *eLife* **11**, e75433 (2022).
33. D. Hoffmann, S. Mereiter, Y. Jin Oh, V. Monteil, E. Elder, R. Zhu, D. Canena, L. Hain, E. Laurent, C. Grünwald-Gruber, M. Klausberger, G. Jonsson, M. J. Kellner, M. Novatchkova, M. Ticevic, A. Chabloz, G. Wirnsberger, A. Hagelkruys, F. Altmann, L. Mach, J. Stadlmann, C. Oostenbrink, A. Mirazimi, P. Hinterdorfer, J. M. Penninger, Identification of lectin receptors for conserved SARS-CoV-2 glycosylation sites. *EMBO J.* **40**, e108375 (2021).
34. K. Lim, G. Nishide, T. Yoshida, T. Watanabe-Nakayama, A. Kobayashi, M. Hazawa, R. Hanayama, T. Ando, R. W. Wong, Millisecond dynamic of SARS-CoV-2 spike and its interaction with ACE2 receptor and small extracellular vesicles. *J. Extracell. Vesicles* **10**, e12170 (2021).
35. T. Ando, N. Kodera, E. Takai, D. Maruyama, K. Saito, A. Toda, A high-speed atomic force microscope for studying biological macromolecules. *Proc. Natl. Acad. Sci.* **98**, 12468–12472 (2001).
36. J. Pallesen, N. Wang, K. S. Corbett, D. Wrapp, R. N. Kirchdoerfer, H. L. Turner, C. A. Cottrell, M. M. Becker, L. Wang, W. Shi, W.-P. Kong, E. L. Andres, A. N. Kettenbach, M. R. Denison, J. D. Chappell, B. S. Graham, A. B. Ward, J. S. McLellan, Immunogenicity and structures of a rationally designed prefusion MERS-CoV spike antigen. *Proc. Natl. Acad. Sci.* **114**, E7348–E7357 (2017).
37. R. Amyot, A. Marchesi, C. M. Franz, I. Casuso, H. Flechsig, Simulation atomic force microscopy for atomic reconstruction of biomolecular structures from resolution-limited experimental images. *PLOS Comput. Biol.* **18**, e1009970 (2022).
38. S. A. McKinney, C. Joo, T. Ha, Analysis of Single-Molecule FRET trajectories using Hidden Markov Modeling. *Biophys. J.* **91**, 1941–1951 (2006).
39. M. McCallum, A. C. Walls, J. E. Bowen, D. Corti, D. Veesler, Structure-guided covalent stabilization of coronavirus spike glycoprotein trimers in the closed conformation. *Nat. Struct. Mol. Biol.* **27**, 942–949 (2020).
40. S. M.-C. Gobeil, K. Janowska, S. McDowell, K. Mansouri, R. Parks, K. Manne, V. Stalls, M. F. Kopp, R. Henderson, R. J. Edwards, B. F. Haynes, P. Acharya, D614G mutation alters SARS-CoV-2 spike conformation and enhances protease cleavage at the S1/S2 junction. *Cell Rep.* **34**, 108630 (2021).
41. E. Cameroni, J. E. Bowen, L. E. Rosen, C. Saliba, S. K. Zepeda, K. Culap, D. Pinto, L. A. VanBlargan, A. De Marco, J. Di Julio, F. Zatta, H. Kaiser, J. Noack, N. Farhat, N. Czudnochowski, C. Havenar-Daughton, K. R. Sprouse, J. R. Dillen, A. E. Powell, A. Chen, C. Maher, L. Yin, D. Sun, L. Soriaga, J. Bassi, C. Silacci-Fregnini, C. Gustafsson, N. M. Franko, J. Logue, N. T. Iqbal, I. Mazzitelli, J. Geffner, R. Grifantini, H. Chu, A. Gori, A. Riva, O. Giannini, A. Ceschi, P. Ferrari, P. E. Cippà, A. Franzetti-Pellanda, C. Garzoni, P. J. Halfmann, Y. Kawaoka, C. Hebnér, L. A. Purcell, L. Piccoli, M. S. Pizzuto, A. C. Walls, M. S. Diamond, A. Telenti, H. W. Virgin, A. Lanzavecchia, G. Snell, D. Veesler, D. Corti, Broadly neutralizing antibodies overcome SARS-CoV-2 Omicron antigenic shift. *Nature* **602**, 664–670 (2022).
42. M. McCallum, N. Czudnochowski, L. E. Rosen, S. K. Zepeda, J. E. Bowen, A. C. Walls, K. Hauser, A. Joshi, C. Stewart, J. R. Dillen, A. E. Powell, T. I. Croll, J. Nix, H. W. Virgin, D. Corti, G. Snell, D. Veesler, Structural basis of SARS-CoV-2 Omicron immune evasion and receptor engagement. *Science* **375**, 864–868 (2022).
43. G. Cerutti, Y. Guo, L. Liu, L. Liu, Z. Zhang, Y. Luo, Y. Huang, H. H. Wang, D. D. Ho, Z. Sheng, L. Shapiro, Cryo-EM structure of the SARS-CoV-2 Omicron spike. *Cell Rep.* **38**, 110428 (2022).
44. Z. Cui, P. Liu, N. Wang, L. Wang, K. Fan, Q. Zhu, K. Wang, R. Chen, R. Feng, Z. Jia, M. Yang, G. Xu, B. Zhu, W. Fu, T. Chu, L. Feng, Y. Wang, X. Pei, P. Yang, X. S. Xie, L. Cao, Y. Cao, X. Wang, Structural and functional characterizations of infectivity and immune evasion of SARS-CoV-2 Omicron. *Cell* **185**, 860-871.e13 (2022).
45. M. Wieczór, P. K. Tang, M. Orozco, P. Cossio, Omicron mutations increase interdomain interactions and reduce epitope exposure in the SARS-CoV-2 spike. *iScience* **26**, 105981 (2023).
46. S. Ren, M. Cai, Y. Shi, Z. Luo, T. Wang, Influence of cough airflow characteristics on respiratory mucus clearance. *Phys. Fluids* **34**, 041911 (2022).

47. F. Rico, A. Russek, L. González, H. Grubmüller, S. Scheuring, Heterogeneous and rate-dependent streptavidin–biotin unbinding revealed by high-speed force spectroscopy and atomistic simulations. *Proc. Natl. Acad. Sci.* **116**, 6594–6601 (2019).
48. C. Valotteau, F. Sumbul, F. Rico, High-speed force spectroscopy: microsecond force measurements using ultrashort cantilevers. *Biophys. Rev.* **11**, 689–699 (2019).
49. J. Yin, P. D. Straight, S. M. McLoughlin, Z. Zhou, A. J. Lin, D. E. Golan, N. L. Kelleher, R. Kolter, C. T. Walsh, Genetically encoded short peptide tag for versatile protein labeling by Sfp phosphopantetheinyl transferase. *Proc. Natl. Acad. Sci.* **102**, 15815–15820 (2005).
50. P. Cossio, G. Hummer, A. Szabo, Kinetic ductility and force-spike resistance of proteins from single-molecule force spectroscopy. *Biophys. J.* **111**, 832–840 (2016).
51. C. Gosse, V. Croquette, Magnetic tweezers: micromanipulation and force measurement at the molecular level. *Biophys. J.* **82**, 3314–3329 (2002).
52. D. Kostrz, H. K. Wayment-Steele, J. L. Wang, M. Follenfant, V. S. Pande, T. R. Strick, C. Gosse, A modular DNA scaffold to study protein–protein interactions at single-molecule resolution. *Nat. Nanotechnol.* **14**, 988–993 (2019).
53. G. I. Bell, Models for the Specific Adhesion of Cells to Cells: A theoretical framework for adhesion mediated by reversible bonds between cell surface molecules. *Science* **200**, 618–627 (1978).
54. A. S. De Souza, V. M. De Freitas Amorim, G. D. A. Guardia, F. R. C. Dos Santos, F. F. Dos Santos, R. F. De Souza, G. De Araujo Juvenal, Y. Huang, P. Ge, Y. Jiang, C. Li, P. Paudel, H. Ulrich, P. A. F. Galante, C. R. Guzzo, Molecular dynamics analysis of fast-spreading severe acute respiratory syndrome coronavirus 2 variants and their effects on the interaction with human angiotensin-converting enzyme 2. *ACS Omega* **7**, 30700–30709 (2022).
55. P. Hinterdorfer, W. Baumgartner, H. J. Gruber, K. Schilcher, H. Schindler, Detection and localization of individual antibody-antigen recognition events by atomic force microscopy. *Proc. Natl. Acad. Sci.* **93**, 3477–3481 (1996).
56. C. Rankl, F. Kienberger, L. Wildling, J. Wruss, H. J. Gruber, D. Blaas, P. Hinterdorfer, Multiple receptors involved in human rhinovirus attachment to live cells. *Proc. Natl. Acad. Sci.* **105**, 17778–17783 (2008).
57. F. Stransky, D. Kostrz, M. Follenfant, S. Pomplun, C. Meyners, T. Strick, F. Hausch, C. Gosse, “Use of DNA forceps to measure receptor-ligand dissociation equilibrium constants in a single-molecule competition assay” in *Methods in Enzymology* (Elsevier, 2024; <https://linkinghub.elsevier.com/retrieve/pii/S0076687924000132>), p. S0076687924000132.
58. D. D. Boehr, R. Nussinov, P. E. Wright, The role of dynamic conformational ensembles in biomolecular recognition. *Nat. Chem. Biol.* **5**, 789–796 (2009).
59. E. Di Cera, Mechanisms of ligand binding. *Biophys. Rev.* **1**, 011303 (2020).
60. D. Mannar, J. W. Saville, Z. Sun, X. Zhu, M. M. Marti, S. S. Srivastava, A. M. Berezuk, S. Zhou, K. S. Tuttle, M. D. Sobolewski, A. Kim, B. R. Treat, P. M. Da Silva Castanha, J. L. Jacobs, S. M. Barratt-Boyes, J. W. Mellors, D. S. Dimitrov, W. Li, S. Subramaniam, SARS-CoV-2 variants of concern: spike protein mutational analysis and epitope for broad neutralization. *Nat. Commun.* **13**, 4696 (2022).
61. P. Han, L. Li, S. Liu, Q. Wang, D. Zhang, Z. Xu, P. Han, X. Li, Q. Peng, C. Su, B. Huang, D. Li, R. Zhang, M. Tian, L. Fu, Y. Gao, X. Zhao, K. Liu, J. Qi, G. F. Gao, P. Wang, Receptor binding and complex structures of human ACE2 to spike RBD from omicron and delta SARS-CoV-2. *Cell* **185**, 630–640.e10 (2022).
62. D. Planas, N. Saunders, P. Maes, F. Guivel-Benhassine, C. Planchais, J. Buchrieser, W.-H. Bolland, F. Porrot, I. Staropoli, F. Lemoine, H. Péré, D. Veyer, J. Puech, J. Rodary, G. Baele, S. Dellicour, J. Raymenants, S. Gorissen, C. Geenen, B. Vanmechelen, T. Wawina-Bokalanga, J. Martí-Carreras, L. Cuypers, A. Sève, L. Hocqueloux, T. Prazuck, F. A. Rey, E. Simon-Loriere, T. Bruel, H. Mouquet, E. André, O. Schwartz, Considerable escape of SARS-CoV-2 Omicron to antibody neutralization. *Nature* **602**, 671–675 (2022).
63. S. Temmam, K. Vongphayloth, E. Baquero, S. Munier, M. Bonomi, B. Regnault, B. Douangboubpha, Y. Karami, D. Chrétien, D. Sanamxay, V. Xayaphet, P. Paphaphanh, V. Lacoste, S. Somlor, K. Lakeomany, N. Phommavanh, P. Pérot, O. Dehan, F. Amara, F. Donati, T. Bigot, M. Nilges, F. A. Rey, S. Van Der Werf, P. T.

Brey, M. Eloit, Bat coronaviruses related to SARS-CoV-2 and infectious for human cells. *Nature* **604**, 330–336 (2022).